ARTICLE

Bundling of GaAs Nanowires: A Case of Adhesion-Induced Self-Assembly of Nanowires

Stefania Carapezzi,[†,*] Giacomo Priante,[‡,#] Vincenzo Grillo,[§,⊥] Laurent Montès,[||] Silvia Rubini,[‡] and Anna Cavallini[†]

[†]Department of Physics and Astronomy, University of Bologna, Viale Berti Pichat 6/2, Bologna, I-40127, Italy, [‡]Istituto Officina dei Materiali del CNR, Laboratorio TASC, S.S.14, Km.163.5, Trieste, I-34149, Italy, [§]Istituto Nanoscienze, Via Campi 213/A, Modena, I-41125, Italy, [⊥]CNR-IMEM, Parco delle Scienze 37a, Parma, I-43100, Italy, and [||]IMEP-LAHC, MINATEC, Grenoble University, Giant Innovation Campus, 3 Parvis Louis Néel, Grenoble, F-38016, France.
[#]Present address: CNRS-Laboratoire de Photonique et de Nanostructures, Route de Nozay, F-91460 Marcoussis, France.

ABSTRACT The origin of deflections of semiconductor nanowires (NWs) induced by an electron beam in scanning electron microscopy has been subject to different interpretations. Similarly, the subsequent clumping together of NWs into bundles is frequently observed, but no interpretation has yet been advanced. Here we present results on the bundling of NWs following the intentional bending by an electron beam. Furthermore, we extend the concept of lateral collapse, usually applied to fibrillar architectures mimicking the adhesiveness of natural surfaces (the so-called Gecko effect), to analyze the mechanism of the NW bundle formation. We demonstrate how the geometry of the NW arrays and the mechanical properties of the composing materials govern bundling and how these parameters should be taken into account in the design of NW arrays both for avoiding vertical misalignment when detrimental and for achieving patterning of NW arrays into nanoarchitectures.

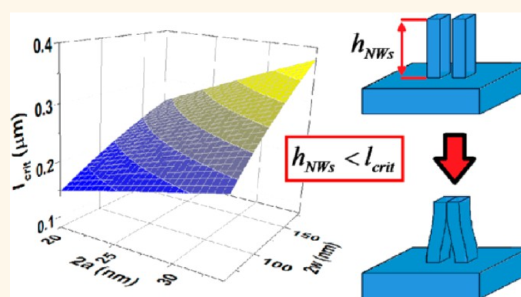

KEYWORDS: nanowire arrays · self-assembly · adhesion · surface engineering · nanoarchitectonics

Semiconductor nanowires (NWs), compared to thin films or their bulk counterparts, offer a wider range of very attractive physical properties enabled by their nanoscale size and surface-to-volume ratio. However, controlled placement of NWs is presently a major challenge for NW-based electronic devices. In particular, vertical alignment with respect to the substrate may be crucial. For instance, vertically aligned (VA) NWs represent natural resonance cavities in lasers without any fabricated mirror,[1] and they lead to wave-guided emission in light-emitting diodes.[2,3] The VA NW architecture is beneficial also for photovoltaic and photodetection applications.[3] In general, direct growth of VA NW arrays on the desired substrate is a way to solve the integration issue for NW-based devices, compared to the aligned transfer of NWs onto a host substrate such as in the Langmuir–Blodgett method.[4]

It is usually taken for granted that orientation of NW arrays is determined by substrate orientation and growth conditions only.[5] For commonly bottom-up fabricated semiconductor NWs, grown *via* metal-assisted vapor–liquid–solid (VLS) or vapor–solid–solid mechanisms,[6] the growth direction is the one that minimizes the total free energy, which is dominated by the surface free energy of the semiconductor–metal interface. NW orientation is thus engineered by the choice of the substrate crystal orientation for epitaxial growth. NW diameter, growth temperature, total pressure, and precursor partial pressure could also control the NW direction.[5]

Nevertheless, NW array orientation may be influenced after growth by further factors. In fact, NWs are pillar-like structures; hence they can bend if sufficiently strong external forces are applied to them. Recently, a few papers about electron-beam-induced bending or self-attraction of ZnO nanorods and NWs[7–9] as well as of GaAs NWs[10,11] have been published. In all these cases the phenomenon has been investigated to determine the nature of the driving

* Address correspondence to stefania.carapezzi2@unibo.it.

Received for review March 12, 2014 and accepted August 27, 2014.

Published online August 27, 2014
10.1021/nn503629d

© 2014 American Chemical Society

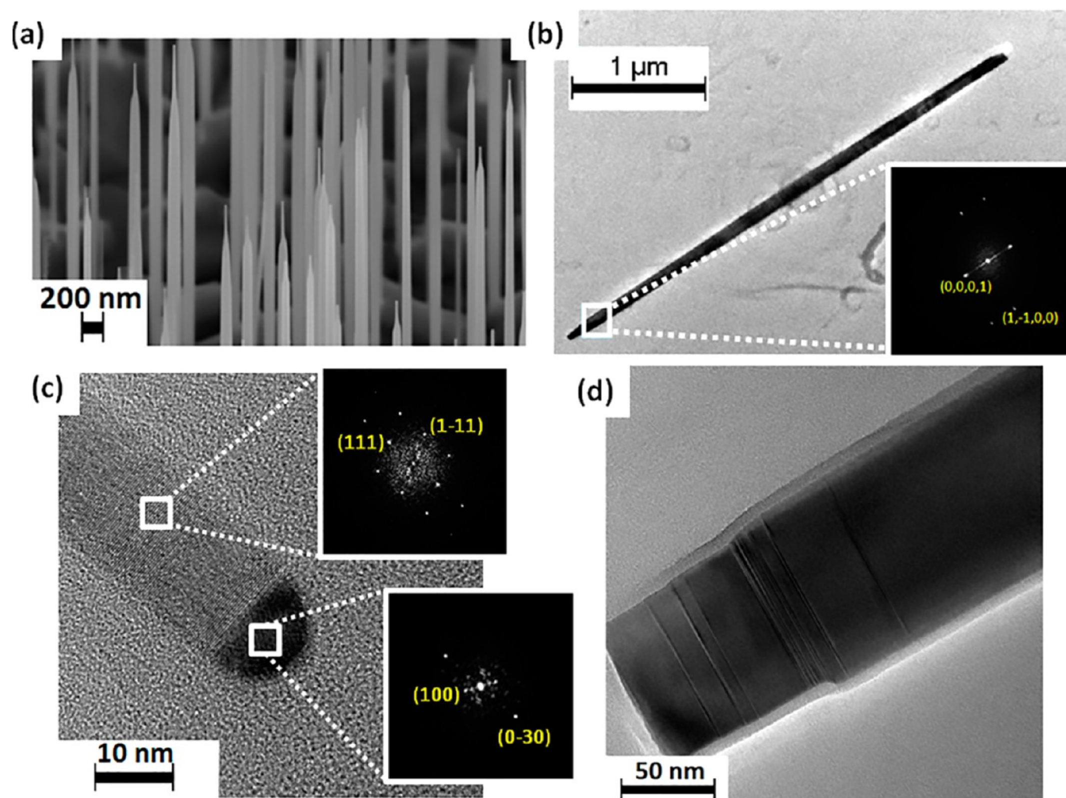

Figure 1. (a) Detail of 45° tilted SEM image of sample A1, showing the characteristic pencil-like tip. (b) Low-magnification TEM image of a representative GaAs NW (sample A1), imaged along the [11$\bar{2}$0] direction. The inset shows a DFT of the same wire in the tip region with the WZ structure. The very tip of the wire was broken, but for another wire it can be seen in (c). (c) High-resolution TEM image of a typical NW head (sample A1). The insets show the DFT from the catalyst NP and from the underneath NW region. The NP's DFT is compatible with hexagonal Au_7Ga_2 down the [0,0,1]; the NW is in this region a cubic ZB structure seen along a ⟨1,1,0⟩ zone axis. (d) High-magnification TEM image of a typical NW body (sample A1), showing the expected oxide layer on the NW surface.

force responsible for the NW bending. Instead, no effort at all has been dedicated to characterize and understand the subsequent formation of NW bundles, their origin, and their stability over time.

In the present work we analyze and discuss the bundling of VLS-grown GaAs NWs consequent to electron-beam-induced bending. We elucidate the springing up of NW bundles as a result of adhesion forces between NW surfaces. To this aim, we generalize the concept of "lateral collapse of fibrils",[15,16] originally developed in the framework of the studies on the adhesiveness of natural contact surfaces.[12] This concept has an important role in modeling the adhesion failure of artificially structured surfaces, called fibrillar architectures, designed to mimic the adhesive skin of lizards and insects.

The key points of our study are (i) the extension of the modeling of fibrillar lateral collapse to NW bundling, to give evidence of how the interplay between mechanical and surface properties of the NWs and the geometrical design of the arrays may lead to a bundling effect, and (ii) the suggestion of ways to control the NW bundling effect. Our work demonstrates how a careful choice of material properties and geometrical design of semiconductor NW arrays matters, when departure from verticality is detrimental for the realization of NW-array-based devices. It also shows that the same factors can turn scanning electron microscopy (SEM) into a new patterning tool, allowing for the nanoscale fine-tuning of the morphology of NW arrays, when the aim is to purposefully induce NW clustering.

In situ, controlled assembling of NWs is indeed a way to realize complex hierarchical surface structures. Recent studies[17] have shown how the aggregation of nanoscale features resulting in sophisticated texturizing of surface morphology leads to the possibility of designing physical properties such as wetting,[18] adhesion,[19] and electrical[20] and thermal transport[21] as well as of directing cell and tissue growth.[22,23] From the technological point of view, the achievement of definite control over the nanoscale design of NW-decorated surfaces, combined with the physical properties of semiconductor materials, may pave the way toward the fabrication of novel smart surface devices.

RESULTS AND DISCUSSION

Clustering of GaAs NWs under Electron Beam Scanning. We have first considered two gold-assisted GaAs NW array samples (samples A1 and A2; growth details are

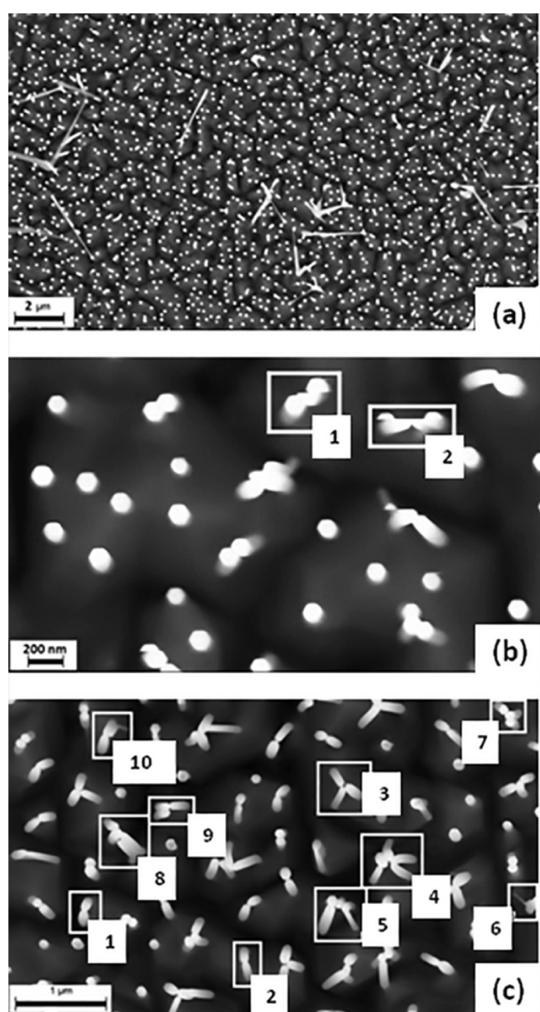

Figure 2. Plan views of sample A1. (a) The micrograph of the GaAs NWs after the growth shows that most of them are VA. (b) The white squares labeled 1 and 2 evidence GaAs NWs that changed their position in between one raster scanning line and the following one. (c) The white squares labeled 1 and 2 highlight the lateral collapse of couples of GaAs NWs. The white square labeled 3 evidences the occurrence of a triangular configuration. More complex geometries also appear (white squares labeled 4−10).

described in the Methods section) differing only by Si doping. They consist of sets of randomly located VA-grown NWs (Figures 1a and 2a). The NWs' morphology of samples A1 and A2 is the same. The NWs show pencil-like tips (Figure 1a), characteristic of the diffusion-limited VLS mechanism.[24] Their average length is about 4.5 μm, and their average diameter is 90 nm, while the tip diameter is about 20 nm. Figure S1a,b of the Supporting Information (SI) quantifies the morphological characterization of these GaAs NWs. Figure 1b shows a representative low-magnification transmission electron microscopy (TEM) image of a NW imaged along the $[11\bar{2}0]$ direction and a diffractogram (DFT; Fourier transform of a high-resolution image) of the same wire in the tip region. Except for a few zincblende (ZB) and stacking fault insertions, most of NWs remain wurtzite (WZ) type along their whole length. Figure 1c shows a high-resolution image of the region including the tip. The image shows lattice fringes for both the NW and the nanoparticle (NP). The tip composition is compatible with a Au_7Ga_2 phase in the [0,0,1] zone axis. Besides, in this region the NW shows a ZB structure. Figure 1d is an image of a NW in the proximity of a breaking point. Some staking faults/twins are clearly visible. Furthermore, the presence of an oxide layer on the surface of the NW is observed.

The SEM investigation of samples A1 and A2 revealed that at the beginning of the observations the large majority of the NWs are VA (Figure 2a), as expected from the growth on the GaAs (111)B substrate.[25] At each raster scanning the bending of a few GaAs NWs occurs (Figure 2b). As the scanning time increases, the number of NW clusters increases (Figure 2c). Figures 2c and Figure 3 are representative SEM micrographs of sample A1 and A2, respectively, where NW bundles coexist with VA NWs. No difference in bending behavior and/or bundling formation between samples A1 and A2 has been observed, suggesting that doping does not affect these mechanisms. An extended discussion on literature results and interpretations of the bending induced by the scanning electron beam and on their comparison to our results as well as a quantitative study of the statistical distribution of the bending forces on GaAs NWs in our samples A1 and A2 is reported in the SI.

Nanowire Bundling: A Case of Lateral Collapse. *Lateral Collapse Theory for Fibrillar Structures.* As abovementioned, in recent years the self-adhesion of adjacent micro/nanopillars has been investigated,[12−15] given its relationship with the adhesive efficiency of artificial fibrillar architectures. The simplest ideal fibrillar structure is modeled as an array of pillars (fibrils) protruding from a substrate (Figure 4a). Each pillar is characterized by its Young's modulus E, moment of inertia I, length h, and squared cross sections of a side $2a$. The pillars are at a distance $2w$ from each other. If two neighboring pillars are brought into contact, they may "laterally collapse", that is, clump together, under the influence of van der Waals forces (Figure 4b).[15,16]

A criterion for the occurrence of this lateral collapsing has been established[15,16] by means of energy balance considerations. When two adjacent pillars adhere, the system is in equilibrium because the adhesion between their two contacting surfaces is (at least) equal to the elastic force of their deformation. The whole elastic strain energy U of the system is accumulated in the noncontact region of length l where bending deformation occurs (Figure 4b) and can be evaluated by the Euler−Bernoulli beam theory.[16,26] If the length of the noncontact region between the two collapsed fibrils increases by a small amount dl, that is, $l \rightarrow l + dl$, then a reduction in the strain energy dU occurs, and under equilibrium condition it must be equal to the work dW needed to decrease the contact area.

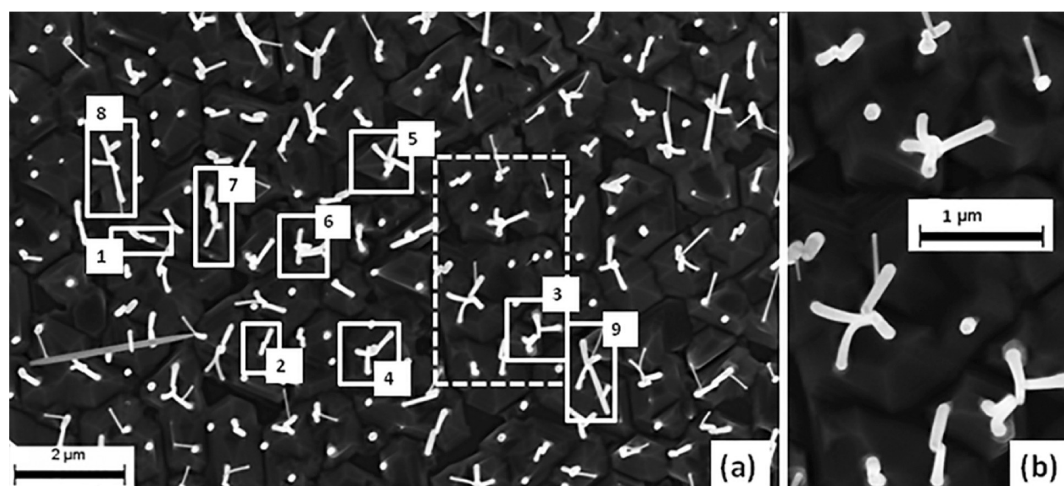

Figure 3. (a) Plan view SEM micrograph of sample A2. Typical NW clusters are labeled as follows: 1 and 2 show the lateral collapse of a couple of GaAs NWs; 3 and 4 are representative of larger NW clusters; 5–9 show more complex geometries. (b) Higher magnification of the area enclosed in the dashed square of (a).

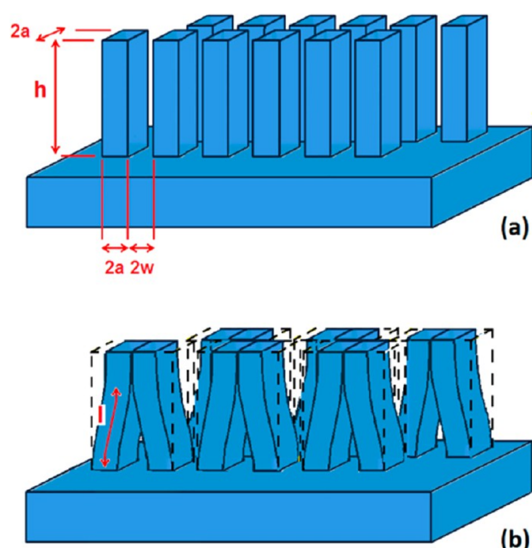

Figure 4. (a) Schematic of a squared cross-section fibrillar structure. (b) Lateral collapse of neighboring pillars.

By equating the two terms dU and dW, one determines the "critical" value l_{crit}:[16]

$$l_{crit} = 2\left(\frac{3Ea^3w^2}{2\gamma_s}\right)^{1/4} \tag{1}$$

where γ_s is the surface energy of the material composing the pillars. Evidently, for fibrils whose height h is smaller than l_{crit} the adhesion is insufficient to balance the elastic force of their bending, and the fibrils bounce back to their nondeformed state. Thus, the "condition for lateral stability" may be expressed as $h < l_{crit}$.[15] Conversely, when the pillar height h satisfies the inequality $h > l_{crit}$, the lateral collapse of two adjacent pillars is possible.

We have proceeded in this framework to study the collapse of GaAs NWs. To this purpose, it is needed to estimate the parameter l_{crit} of our samples and compare it to the NWs' average height in order to check the fulfillment of the lateral collapse condition. To evaluate l_{crit}, it is not possible to make use of eq 1 because (i) the cross-section of the NWs is not squared and (ii) the NWs are not located in a regular pattern. Therefore, we have modified the procedure of Glassmaker *et al.*[15] and Hui *et al.*[16] as follows. First, we have accounted for the actual shape of the GaAs NWs under test, which have a hexagonal cross-section (Figure 1b). By the above illustrated approach, we have estimated the total strain energy U for the system of two bent NWs as[11,26]

$$U = 2\int_0^l \frac{M^2}{2EI_{hex}}dy = \frac{15\sqrt{3}a^4E}{16l^3}w^2 \tag{2}$$

where M is the bending moment, I_{hex} is the moment of inertia of a hexagonal cross-sectional pillar, and a is the side of the hexagon. By equating the strain energy variation dU due to a small length variation dl of the noncontact region between two adhered pillars to the work dW necessary for decreasing their contact area, we have obtained the new criterion for the lateral collapse:

$$h > l_{crit} = \left(\frac{45\sqrt{3}a^3Ew^2}{32\gamma_s}\right)^{1/4} \tag{3}$$

Equation 3 holds for ideal fibrillar architectures whose fibrils have hexagonal cross-sections and are located in a regular pattern at the distance $2w$ from each other. However, the GaAs NW arrays of our samples do not have a regular pattern (Figure 2a); hence the parameter $2w$ is not well defined. To solve this issue, we have elaborated a procedure to apply the critical length concept even in the case of randomly distributed NWs.

Estimation of the Critical Length for Randomly Located NWs. We have processed plan view SEM images (Figure 5a) of the unbundled arrays by means of ImageJ software[27] to generate point maps (Figure 5b) representing the spatial distribution of the NWs. Then, we

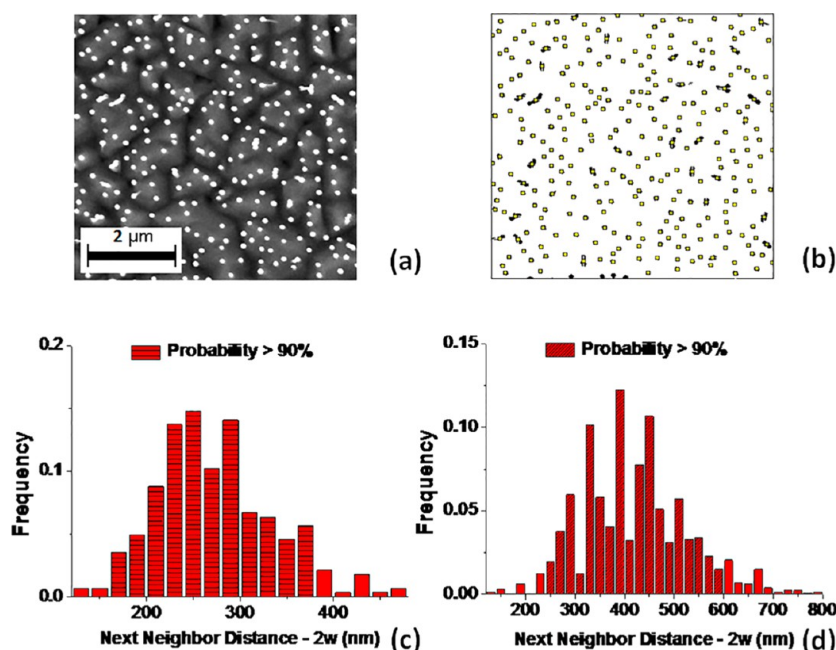

Figure 5. (a) Typical plan view SEM image of VA GaAs NWs of sample A1 and (b) the correspondent spatial point map. Histograms of the frequency distributions of the nearest neighbor distance 2*w* among the GaAs NWs of samples A1 (c) and A2 (d), respectively. The range where more than 90% of values lie is evidenced by cross-hatched columns. The two distributions have the same bin size (20 nm) to easily compare them.

TABLE 1. Range of Values of γ_s, E, and E/γ_s of WZ GaAs

γ_s (J/m^2)	E (GPa)	E/γ_s (m^{-1})
0.86[41]	134[38]	1.55×10^{11}
1.5[42,43]	134[38]	8.9×10^{10}

have used the package Spatstat[28] for the R language[29] to statistically analyze the point patterns and compute the distance of each point from its nearest neighbor. The full description of the procedure is given in the SI. The most natural generalization of the parameter 2*w* in the case of randomly spaced NWs is the distribution of the nearest neighbor distances (Figure 5c,d).

To evaluate the critical length in eq 3, the ratio E/γ_s is also needed. Even if research on the elastic properties of NWs has lately attracted much interest,[30] up to now very few studies on Young's modulus of GaAs NWs have been carried out, and the experimental results are not conclusive. For instance, Young's modulus for ZB GaAs NWs has been reported to span from 30 to 38 GPa.[31] Other authors report that *E* increases as the NW's diameter decreases,[32] consistently with the elastic behavior of other semiconductor NWs,[33,34] with values ranging from 118 to 183 GPa. The values of *E* reported by Wang *et al.*[32] for NWs comparable to ours are in good agreement with Young's modulus of bulk ZB GaAs.[35] Even if our NWs show prevailing WZ crystal structure (Figure 1b), we do not expect their mechanical properties to be significantly different from ZB ones. In fact, although bulk WZ GaAs is only occasionally reported,[36] theoretical calculations show that its mechanical behavior should be similar to that of ZB.

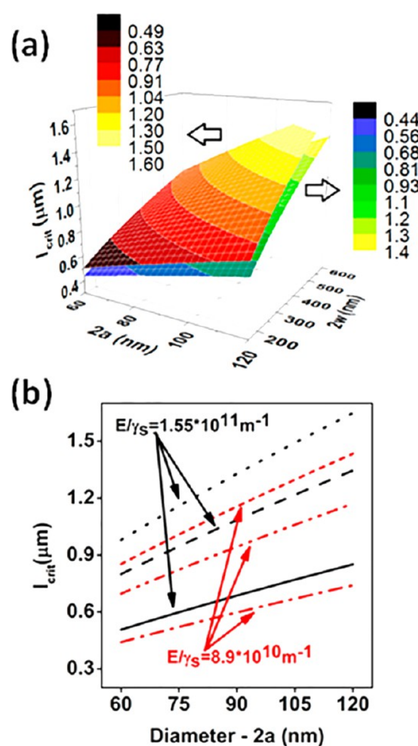

Figure 6. (a) Plots of the critical length l_{crit} *versus* the diameter 2*a* (ranging from 60 to 120 nm; compare with Figure S1a,b) and the distance 2*w* between the NWs (ranging from 160 to 600 nm; compare with Figure 5c,d) for $E/\gamma_s = 1.55 \times 10^{11}$ m^{-1} and for $E/\gamma_s = 2 \times 10^{10}$ m^{-1}. (b) Projections of the critical length l_{crit} for three values of the distance 2*w* with $E/\gamma_s = 1.55 \times 10^{11}$ m^{-1} and $E/\gamma_s = 2 \times 10^{10}$ m^{-1}, respectively. Black solid and red dot-dashed lines correspond to 2*w* = 160 nm, black dashed and red dot-dot-dashed lines correspond to 2*w* = 400 nm, and black dotted and red short dashed lines correspond to 2*w* = 600 nm.

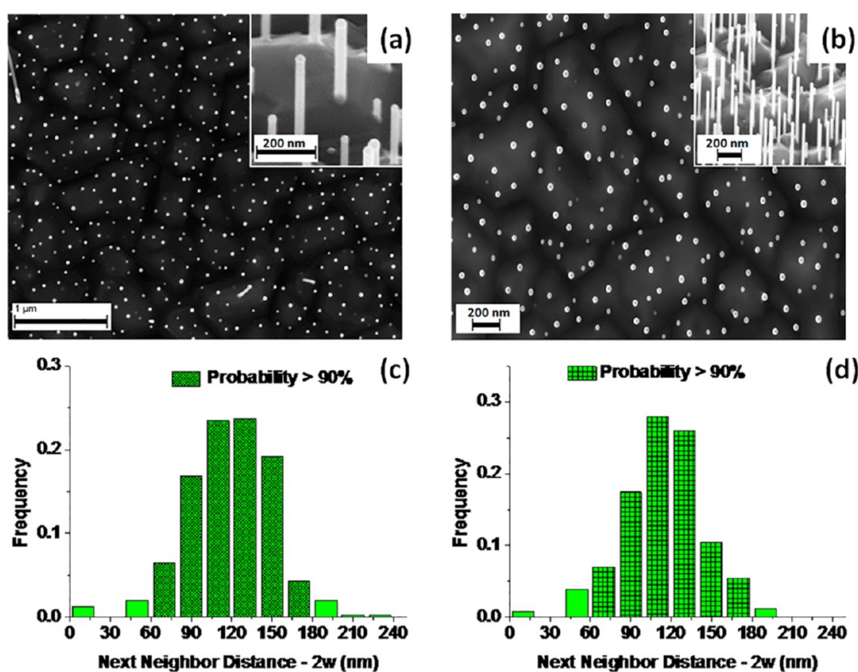

Figure 7. SEM micrographs of samples B1, B2: (a, b) Plan views. The corresponding 45° tilted views are insets. Histograms of the frequency distributions of the nearest neighbor distance 2*w* among the GaAs NWs of samples B1 (c) and B2 (d), respectively, are also shown. The range where more than 90% of values lie is evidenced by cross-hatched columns. The two distributions have the same bin size (20 nm) to easily compare them.

In particular, the difference in the bulk modulus should not be larger than 1%.[37] The calculation of Young's modulus of WZ GaAs is extensively reported in the SI.

Recently, *in situ* compression tests over single GaAs NWs with three different kinds of crystal structures (ZB, WZ, and WZ with a high density of stacking faults, whose spatial periodicity was of 1–5 nm) have been carried out.[38] Experimental load–displacement curves have been reported in order to investigate the critical load at which GaAs NWs buckle. By means of the Euler formula

$$P_{cr} = \frac{\pi^2 EI_{hex}}{(Kh)^2} \quad (4)$$

where K is the NW effective length factor, accounting for the boundary conditions (K = 0.5 because both NW's ends are fixed[38]), it is possible to determine Young's modulus of NWs from load–displacement plots. Chen *et al.*[38] performed this analysis only for ZB GaAs NWs, because the focus of their work was on the deformation behavior of GaAs NWs. We considered it a precious opportunity the possibility to access the experimental estimate of Young's moduli of WZ GaAs NWs, since no published data on them exist. Consequently, (i) we digitized the above-mentioned experimental plots (compare the original graph in Figure S7a with the digitized one in Figure S7b), (ii) we estimated P_{cr} (Figure S7b,c), and (iii) we calculated Young's moduli values by applying eq 4. It is worth noting that the geometrical sizes of probed NWs are reported[38] to be about 60 nm for the diameter and about 6.5:1 for the aspect ratio of length to diameter. The values of Young's moduli extracted are 134 GPa for pure WZ GaAs NWs and 200 GPa for WZ GaAs NWs with a high density of stacking faults. The value of 134 GPa is in good agreement with the values of Young's modulus of WZ GaAs we have reported in Table S-1 of the SI. GaAs NWs of samples A1 and A2 present only a few stacking fault insertions (Figure 1b,d). Then, in our calculation we have adopted the value of 134 GPa for determining the critical length. According to these findings, the presence of stacking faults is responsible not only for the reduction of brittleness of GaAs NWs, as already pointed out by Chen *et al.*,[38] but also for the enhancement of their stiffness. A higher density of stacking faults could explain why few GaAs NWs of samples A1 and A2 remain unbent after prolonged electron beam exposure (Figures 2c and 3).

The experimental determination of the surface energy of GaAs NWs has not been performed yet. Only one theoretical study concerning the surface energy of metallic NWs has been published.[39] A size dependence of the surface energy has been therein reported, with a departure from bulk values when the NWs' diameter is smaller than 10 nm.[39] Since the average diameter of our GaAs NWs is about 90 nm, then WZ bulk GaAs surface energy may be confidently used in eq 3. Similarly, with respect to Young's modulus, experimental data on the bulk surface energy of the hexagonal phase are not available, while theoretical models have been proposed.[40] The calculations show that the $(11\bar{2}0)$ surface in the III–V hexagonal phase is similar

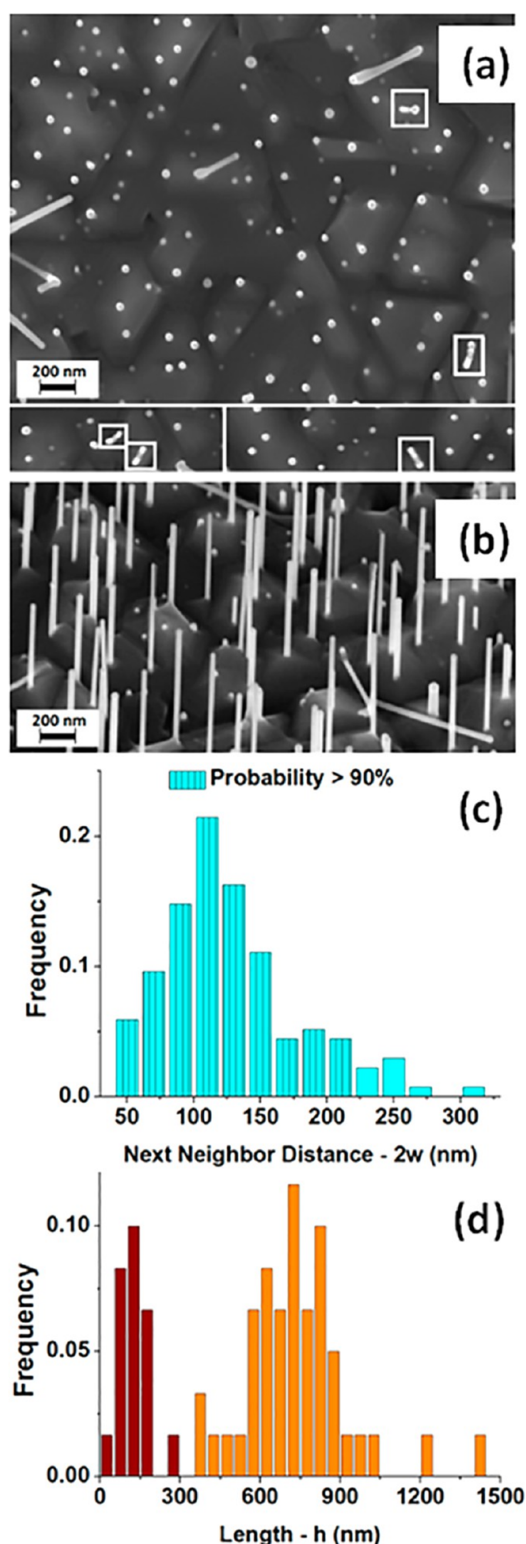

Figure 8. SEM micrographs of sample C. (a) Typical plan view; (b) corresponding 33.2° tilted view. In (a) some laterally collapsed NWs are framed within white rectangles. Histograms of the frequency distribution of the nearest neighbor distance 2*w* among the GaAs NWs (c) (the range where more than 90% of values lies is evidenced by cross-hatched columns; bin size 20 nm) and of the frequency distribution of NWs' lengths *h* (d) (bin size 50 nm).

to the (110) surface in the III–V cubic phase;[40] hence we used the experimental determinations of γ_s relevant to the ZB GaAs (110) surface.[41–43]

Given the dispersion of values of γ_s, in eq 3 we used the maximum and minimum values available for E/γ_s (Table 1) to evaluate how the above-mentioned variability affects the calculation of the critical length.

Figure 6a shows the values of the critical length l_{crit} over the ranges of values that $2w$ (Figure 5c,d) and $2a$ (Figure S1a,b) may assume, for each of the two extreme values of E/γ_s (Table 1). To evaluate more clearly the behavior of l_{crit} *versus* the parameters $2w$ and $2a$, the projections of l_{crit} for three representative values of $2w$ are plotted in Figure 6b.

It is worth noting that the calculated values of l_{crit} are significantly smaller than the average NW height, whatever the actual value of the parameters. In fact, the highest possible value of l_{crit} is 1.65 μm (Figure 6a), well below the average GaAs NW height of 4.5 μm. Therefore, the condition expressed by the inequality of eq 3 is satisfied, which is in agreement with our experimental observations of NW bundles.

To corroborate the validity of the lateral collapse criterion for the NW bundling formation, we characterized further arrays of intrinsic GaAs NWs (samples B1, B2, and C) grown for briefer times than samples A1 and A2. These NWs are shorter, thinner, and untapered. Their density is higher, since the Au layer used to assist their growth was thicker (growth details are reported in the Methods section). Figure 7a,b show SEM micrographs of samples B1 and B2, while Figure 8a,b are SEM micrographs of sample C. The average length of the NWs is 240 nm for sample B1 and 455 nm for sample B2. The average diameter is about 27 nm for all these NWs. As regards sample C, its NWs present two different length distributions (Figure 8d), with average lengths of 125 and 740 nm, respectively. Their average diameter is 35 nm.

In agreement with previous literature reports on GaAs NWs of the same diameter,[32] the value E = 183 GPa has been used here to evaluate the critical length for samples B1, B2, and C. Figure 9a shows the plots of l_{crit} *versus* $2a$ and $2w$ for the two values of γ_s reported in Table 1 for samples B1 and B2, which possess similar intervals of values $2a$ (compare with Figure S1c,d) and $2w$ (compare with Figure 7c,d). Figure 9b shows the plots of l_{crit} *versus* $2a$ and $2w$ for the two values of γ_s reported in Table 1 for sample C. It is noteworthy to observe that the presence of two different distributions of lengths for the NWs of sample C does not affect the critical length value, which depends exclusively on the spatial locations and the diameters of NWs (see eq 3).

In contrast to samples A1 and A2, no NW bundling occurs in samples B1 and B2 (Figure 7a,b), while some bundles occur in sample C. In Figure 8a the laterally collapsed NWs are framed within white rectangles. The general observation is that the lateral collapse occurs

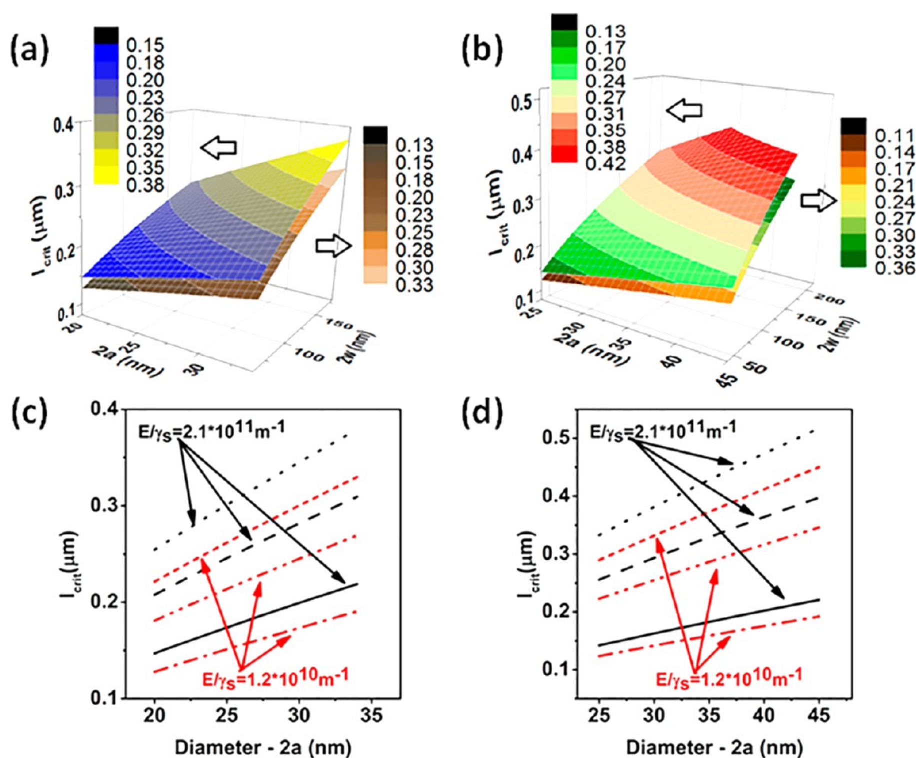

Figure 9. (a, b) Plots of the critical length l_{crit} *versus* the diameter 2*a* and the distance 2*w* between the NWs for E = 183 GPa and for both γ_s = 0.86 J/m^2 (upper surface) and γ_s = 1.5 J/m^2 (lower surface). In (a) 2*a* ranges from 20 to 34 nm (compare with Figure S1c,d) and 2*w* ranges from 60 to 180 nm (compare with Figure 7c,d). In (b) 2*a* ranges from 25 to 45 nm (compare with Figure S1e) and 2*w* ranges from 40 to 220 nm (compare with Figure 8c). (c, d) Projections of the critical length l_{crit} for three values of the distance 2*w* with $E/\gamma_s = 2.1 \times 10^{11}$ m^{-1} and $E/\gamma_s = 1.2 \times 10^{11}$ m^{-1}, respectively. In (c) black solid and red dot-dashed lines correspond to 2*w* = 60 nm, black dashed and red dot-dot-dashed lines correspond to 2*w* = 130 nm, and black dotted and red short dashed lines correspond to 2*w* = 180 nm. In (d) black solid and red dot-dashed lines correspond to 2*w* = 40 nm, black dashed and red dot-dot-dashed lines correspond to 2*w* = 120 nm, and black dotted and red short dashed lines correspond to 2*w* = 220 nm.

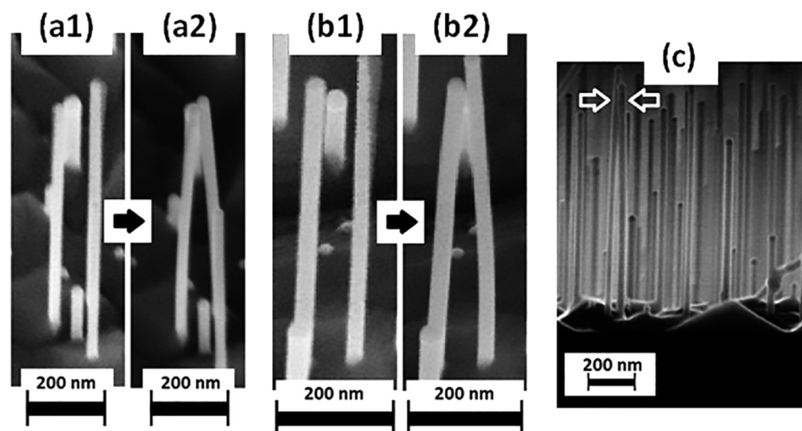

Figure 10. SEM micrographs of sample C. (a1, a2 and b1, b2) Lateral collapsing of NWs subsequent to electron beam exposure: in (a1) and (b1) each NW is still upright, in (a2) and (b2) the NWs are bundled. For (a1,a2) $h_{NWleft} \approx 950$ nm $\approx h_{NWright}$, for (b1,b2) $h_{NWleft} \approx 910$ nm, $h_{NWright} \approx 840$ nm. (a1,a2) and (b1,b2) are 33.2° tilted views. (c) Cross sectional view of sample C. White arrows highlight a couple of collapsed NWs ($h_{NWleft} \approx 1874$ nm, $h_{NWright} \approx 1706$ nm).

for the NWs with a very small interdistance. Figure 10 shows other examples of observed bundles in sample C. All collapsed NWs have heights that are larger than the critical length evaluated for sample C (Figure 9b).

Thus, we can assess that in all the NW arrays investigated no violation of the lateral collapse criterion has ever been observed.

Finally, we have investigated the stability over time of the NW bundles. This issue is of major importance in view of both (i) unwanted misalignment detrimental to technological implementations and (ii) purposefully induced NW bundling as a way to texturize NW arrays. In the literature this investigation has been performed by reusing SEM[7] just 1 week after the NW bundle formation.

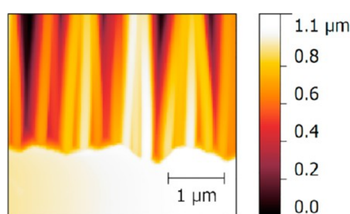

Figure 11. Cross-sectional AFM micrograph of sample A1 (semicontact mode) obtained two months after the SEM characterization.

To check the bundling stability, two months after the SEM imaging we performed atomic force microscopy (AFM) characterization of samples A1 and A2 in a cross-sectional configuration. Probing the NW arrays by AFM was chosen as an alternative method to SEM in order to rule out any perturbation related to the use of an electron beam. In Figure 11 a representative AFM topographic image of sample A1 is shown, confirming the stability in time at ambient conditions of the bundles.

CONCLUSIONS

In this work we reported on the formation of bundles of gold-assisted, prevailing WZ, both doped and intrinsic GaAs NWs exposed to a SEM electron beam. We analyzed the NW bundle formation by extending the theory of lateral collapse of fibrillar structures to semiconductor NWs. We successfully adapted the classical mechanics' concept of critical length, and we showed that it is still a good indicator to describe and predict the bundling of semiconductor NWs in our samples, even down to very small NW sizes. We have drawn some conclusions from our findings. First, lateral collapse induced by surface forces can occur between adjacent VA NWs depending on the material properties and on the geometry of the array. In addition, this clustering, once occurred, lasts in time. The existence of a threshold in the NWs' length and in their distance must be taken into account when devising the growth of VA NW arrays for technological applications where misalignment is detrimental. The lateral collapse of NWs presents also a positive potential as regards the possibility to turn SEM into a fine patterning tool for the design of anisotropic surface architectures, which may enable the fabrication of novel smart surface devices.

METHODS

Growth Details. VA GaAs NWs have been grown by gold-assisted solid-source molecular beam epitaxy (MBE) on n-type $n = 10^{18}$ cm^{-3} GaAs (111)B wafers.[44] Au has been deposited at room temperature into a metallization chamber connected in ultrahigh vacuum to the MBE system after thermal deoxidation of the GaAs substrate. Then, the NWs have been grown at 580 °C, with an As/Ga beam-equivalent pressure ratio of 12, using a Ga flux value that yields an equivalent two-dimensional GaAs growth rate of 1 μm/h. The Au thickness was 0.02 nm in the case of samples A1 and A2, 0.2 nm for samples B1 and B2, and 0.1 nm for sample C. The resulting NW density is of 6.4×10^8 NWs/cm^2 for sample A1, 2.6×10^8 NWs/cm^2 for sample A2, about 4×10^9 NWs/cm^2 for both samples B1 and B2, and 8.1×10^8 NWs/cm^2 for sample C. Growth time was 60 min for samples A1 and A2, 20 min for samples B1 and B2, and 30 min for sample C. All samples were nonintentionally doped, except sample A2, which was doped during the growth by coevaporation of Si, giving a weakly p-type character to the NWs.[44]

Characterization Methods. The NW morphology and their bending/bundling have been studied by SEM, using a Zeiss SUPRA 40 and a Zeiss LEO 1530 field emission SEM, using an acceleration voltage of 5 and 10 kV. The NW morphology and their bundling have been investigated also by AFM, using a Dimension-3100 with a Nanoscope4 controller from Bruker (Veeco). Finally, the structural information has been achieved by means of TEM analyses using a JEOL 2200 with Scherzer resolution of 0.19 nm. For TEM experiments the wires were mechanically transferred from the original substrate onto a carbon-coated copper mesh.

Conflict of Interest: The authors declare no competing financial interest.

Supporting Information Available: Additional material as discussed in the text. This material is available free of charge *via* the Internet at http://pubs.acs.org.

REFERENCES AND NOTES

1. Huang, M. H.; Mao, S.; Feick, H.; Yan, H.; Wu, Y.; Kind, H.; Weber, E.; Russo, R.; Yang, P. Room-Temperature Ultraviolet Nanowire Nanolasers. *Science* **2001**, *292*, 1897–1899.
2. Könenkamp, R.; Word, R. C.; Schlegel, C. Vertical Nanowire Light-Emitting Diode. *Appl. Phys. Lett.* **2004**, *85*, 6004–6006.
3. Wei, W.; Bao, X. Y.; Soci, C.; Ding, Y.; Wang, Z. L.; Wang, D. Direct Heteroepitaxy of Vertical InAs Nanowires on Si Substrates for Broad Band Photovoltaics and Photodetection. *Nano Lett.* **2009**, *9*, 2926–2934.
4. Whang, D.; Jin, S.; Lieber, C. M. Large-Scale Hierarchical Organization of Nanowires for Functional Nanosystems. *Jpn. J. Appl. Phys.* **2004**, *43*, 4465–4470.
5. Fortuna, S. A.; Li, X. Metal-Catalyzed Semiconductor Nanowires: A Review on the Control of Growth Directions. *Semicond. Sci. Technol.* **2010**, *25*, 024005.
6. Wang, N.; Cai, Y.; Zhang, R. Q. Growth of Nanowires. *Mater. Sci. Eng. R* **2008**, *60*, 1–51.
7. Wang, X.; Summers, C. J.; Wang, Z. L. Self-Attraction among Aligned Au/ZnO Nanorods under Electron Beam. *Appl. Phys. Lett.* **2005**, *86*, 013111.
8. Liu, J.; Lee, S.; Lee, K.; Ahn, Y. H.; Park, J.-Y.; Koh, K. H. Bending and Bundling of Metal-Free Vertically Aligned ZnO Nanowires Due to Electrostatic Interaction. *Nanotechnology* **2008**, *19*, 185607.
9. Xinhai, H.; Wang, G.; Zhou, L.; Hou, J. G. Crystal Orientation-Ordered ZnO Nanorod Bundles on Hexagonal Heads of ZnO Microcones: Epitaxial Growth and Self-Attraction. *Chem. Commun.* **2006**, *2*, 212–214.
10. Plissard, S.; Larrieu, G.; Wallart, X.; Caroff, P. High Yield of Self-Catalyzed GaAs Nanowire Arrays Grown on Silicon *via* Gallium Droplet Positioning. *Nanotechnology* **2011**, *22*, 275602.
11. Xing, D.; Dayeh, S. A.; Veeramuthu, V.; Larrue, A.; Wang, J.; Su, H.; Soci, C. Tailoring the Vapor-Liquid-Solid Growth toward the Self-Assembly of GaAs Nanowire Junctions. *Nano Lett.* **2011**, *11*, 4947–4952.
12. Jagota, A.; Hui, C. Y. Adhesion, Friction, and Compliance of Bio-Mimetic and Bio-Inspired Structured Interfaces. *Mater. Sci. Eng. R* **2011**, *72*, 253–292.
13. Lee, D. H.; Kim, Y.; Fearing, R. S.; Maboudian, R. Effect of Fiber Geometry on Macroscale Friction of Ordered Low-Density Polyethylene Nanofiber Arrays. *Langmuir* **2011**, *27*, 11008–11016.

14. Geim, A. K.; Dubonos, S. V.; Grigorieva, I. V.; Novoselov, K. S.; Zhukov, A. A.; Shapoval, S. Y. Microfabricated Adhesive Mimicking Gecko Foot-Hair. *Nat. Mater.* **2003**, *2*, 461–463.
15. Glassmaker, N. J.; Jagota, A.; Hui, C.-Y.; Kim, J. Design of Biomimetic Fibrillar Interfaces; 1 Making Contact. *J. R. Soc. Interface* **2004**, *1*, 23–33.
16. Hui, C. Y.; Jagota, A.; Lin, Y. Y.; Kramer, E. J. Constraints on Microcontact Printing Imposed by Stamp Deformation. *Langmuir* **2002**, *18*, 1394–1407.
17. Tawfick, S.; De Volder, M.; Copic, D.; Park, S. J.; Oliver, C. R.; Polsen, E. S.; Roberts, M. J.; Hart, A. J. Engineering of Micro- and Nanostructured Surfaces with Anisotropic Geometries and Properties. *Adv. Mater.* **2012**, *24*, 1628–1674.
18. Fan, J.; Zhao, Y. Nanocarpet Effect Induced Superhydrophobicity. *Langmuir* **2010**, *26*, 8245–8250.
19. Chen, S.; Soh, A. K. Tuning the Geometrical Parameters of Biomimetic Fibrillar Structures to Enhance Adhesion. *J. R. Soc. Interface* **2008**, *5*, 373–382.
20. Liu, Z. C.; Ci, L. J.; Kar, S.; Ajayan, P. M.; Lu, J. Q. Fabrication and Electrical Characterization of Densified Carbon Nanotube Micropillars for IC Interconnection. *IEEE Trans. Nanotechnol.* **2009**, *8*, 196–203.
21. Warzoha, R. J.; Zhang, D.; Feng, G.; Fleischer, A. S. Engineering Interfaces in Carbon Nanostructured Mats for the Creation of Energy Efficient Thermal Interface Materials. *Carbon* **2013**, *61*, 441–457.
22. Kim, D.-J.; Seol, J.-K.; Lee, G.; Kim, G.-S.; Lee, S.-K. Cell Adhesion and Migration on Nanopatterned Substrates and Their Effects on Cell-Capture Yield. *Nanotechnology* **2012**, *23*, 395102.
23. Qi, S.; Yi, C.; Ji, S.; Fong, C.-C.; Yang, M. Cell Adhesion and Spreading Behavior on Vertically Aligned Silicon Nanowire Arrays. *ACS Appl. Mater. Interfaces* **2009**, *1*, 30–34.
24. Dubrovskii, V. G.; Sibirev, N. V.; Cirlin, G. E.; Tchernycheva, M.; Harmand, J. C.; Ustinov, V. M. Shape Modification of III-V Nanowires: the Role of Nucleation on Sidewalls. *Phys. Rev. E* **2008**, *77*, 1–7.
25. Ohlsson, B. J.; Bjork, M. T.; Magnusson, M. H.; Deppert, K.; Samuelson, L.; Wallenberg, L. R. Size-, Shape-, and Position-Controlled GaAs Nano-Whiskers. *Appl. Phys. Lett.* **2001**, *79*, 3335–3337.
26. Hibbeler, R. C. *Mechanics of Materials*, 3rd ed.; Prentice-Hall: Englewood Cliffs, NJ, 1997.
27. Rasband, W. S. *ImageJ*; U.S. National Institutes of Health: Bethesda, MD, USA, imagej.nih.gov/ij/, 1997−2012.
28. Baddeley, A.; Turner, R. spatstat: an R Package for Analyzing Spatial Point Patterns. *J. Stat. Software* **2005**, *12*, 1−42. URL: www.jstatsoft.org/.
29. R Core Team (2013). R: a Language and Environment for Statistical Computing. R Foundation for Statistical Computing, Vienna, Austria, URL http://www.R-project.org/.
30. Hanbücken, M.; Müller, P.; Wehrspohn, R. B. *Mechanical Stress on the Nanoscale*; Wiley-VCH Verlag & Co. KGaA: Weinheim, 2011.
31. Alekseev, P. A.; Dunaevskii, M. S.; Stovpyaga, A. V.; Lepsa, M.; Titkov, A. N. Measurement of Young's Modulus of GaAs Nanowires Growing Obliquely on a Substrate. *Semiconductors* **2012**, *46*, 641–646.
32. Wang, Y.-B.; Wang, L.-F.; Joyce, H. J.; Gao, Q.; Liao, X.-Z.; Mai, Y.-W.; Tan, H. H.; Zou, J.; Ringer, S. P.; Gao, H.-J.; *et al.* Super Deformability and Young's Modulus of GaAs Nanowires. *Adv. Mater.* **2011**, *23*, 1356–1360.
33. Chen, C. Q.; Shi, Y.; Zhang, Y. S.; Zhu, J.; Yan, Y. J. Size Dependence of Young's Modulus in ZnO Nanowires. *Phys. Rev. Lett.* **2006**, *96*, 075505.
34. Stan, G.; Ciobamu, C. V.; Parthangal, P. M.; Cook, R. F. Diameter-Dependent Radial and Tangential Elastic Moduli of ZnO Nanowires. *Nano Lett.* **2007**, *7*, 3691–3697.
35. Adachi, S., Ed. *Properties of Aluminium Gallium Arsenide*; EMIS Data Reviews Series No. 7; INSPEC; The Institution of Electrical Engineers: London, 1993.
36. McMahon, M. I.; Nelmes, R. J. Observation of a Wurtzite Form of Gallium Arsenide. *Phys. Rev. Lett.* **2005**, *95*, 215505.
37. Bechstedt, J.; Belabbes, A. Structure, Energetics, and Electronic States of III−V Compound Polytypes. *J. Phys.: Condens. Matter* **2013**, *25*, 273201.
38. Chen, B.; Wang, J.; Gao, Q.; Chen, Y.; Liao, X.; Lu, C.; Hoe Tan, H.; Mai, Y.-W.; Zou, J.; Ringer, S. P.; *et al.* Strengthening Brittle Semiconductor Nanowires through Stacking Faults: Insights from *in Situ* Mechanical Testing. *Nano Lett.* **2013**, *13*, 4369–4373.
39. Ouyang, G.; Li, X. L.; Tan, X.; Yang, G. W. Surface Energy of Nanowires. *Nanotechnology* **2008**, *19*, 045709.
40. Sibirev, N. V.; Timofeeva, M. A.; Bol'shakov, A. D.; Nazarenko, M. V.; Dubrovskii, V. G. Surface Energy and Crystal Structure of Nanowhiskers of III−V Semiconductor Compounds. *Phys. Solid State* **2010**, *52*, 1531–1538.
41. Messmer, C.; Bilello, J. C. The Surface Energy of Si, GaAs, and GaP. *J. Appl. Phys.* **1981**, *52*, 4623–4629.
42. Cahn, J. W.; Hanneman, R. E. (111) Surface Tensions of III−V Compounds and Their Relationship to Spontaneous Bending of Thin Crystals. *Surf. Sci.* **1964**, *1*, 387–398.
43. Stekolnikov, A. A.; Bechstedt, F. Shape of Free and Constrained Group-IV Crystallites: Influence of Surface Energies. *Phys. Rev. B* **2005**, *72*, 125326.
44. Piccin, M.; Bais, G.; Grillo, V.; Jabeen, F.; De Franceschi, S.; Carlino, E.; Lazzarino, M.; Romanato, F.; Businaro, L.; Rubini, S. A.; *et al.* Growth by Molecular Beam Epitaxy and Electrical Characterization of GaAs Nanowires. *Phys. E (Amsterdam, Neth.)* **2007**, *37*, 134–137.